Antiphase boundaries in *B*2 intermetallics: Proximate structures, formation energies, and chemical stability

Justin A. Mayer● and Tresa M. Pollock ●

Materials Department, University of California Santa Barbara, Santa Barbara, California 93106, USA

K. V. Vamsi ●

Department of Metallurgical Engineering and Materials Science, Indian Institute of Technology Indore, Indore 453552, India

Ram Seshadri ●

Materials Department, University of California Santa Barbara, Santa Barbara, California 93106, USA
and Department of Chemistry and Biochemistry, University of California, Santa Barbara, California 93106, USA

Multiphase bcc/*B*2-based alloy systems have recently received considerable attention because their microstructures are often remarkably similar to the γ/γ' microstructure of Ni-based superalloys. The underlying plastic deformation mechanisms of bcc-based intermetallics, however, are not well understood across the composition space where they are thermodynamically stable. Within this contribution, we analyze deformation of *B*2 intermetallics to develop a reliable platform for efficiently predicting antiphase boundary energies and the associated fault widths as a function of elemental substitution on a particular lattice site of the intermetallic. To achieve this we extend the diffuse multilayer fault model to predict close packed structures that recreate the bonding environment within the layers adjacent to the $\frac{1}{2}\langle 111 \rangle \{110\}$ antiphase boundary of the *B*2 intermetallic. Specifically, the impact of elemental substitution on both antiphase boundary energy and fault width is presented for $\mathrm{Hf}_{1-x}\mathrm{Ti}_x\mathrm{Ru}$ and $\mathrm{Hf}_{1-x}\mathrm{Al}_x\mathrm{Ru}$ and the implications of our findings are discussed. We also highlight a simple bonding model for transition metal-based *B*2 intermetallics that explains their chemical stability and large antiphase boundary energies. The results presented here offer insight into both the nature of plastic deformation within the *B*2 intermetallic and the important underlying chemical concepts that can potentially be leveraged to aid in the design of bcc-based alloy systems that rival Ni-based γ/γ' microstructures.

I. INTRODUCTION

There has been a significant effort devoted to developing novel metallic alloys that exceed the thermomechanical properties of conventional Ni-based superalloys. Considering the success of the $\gamma \backslash \gamma'$ microstructure, a particularly enticing solution to the challenge at hand is to mimic this microstructure within novel alloy systems. In particular, refractory alloys (i.e., alloys containing Ti, V, Cr, Zr, Nb, Mo, Hf, and/or W) are viewed as promising candidates for next generation high temperature structural materials [1,2]. These alloys form a disordered body centered cubic lattice (referred to as the *A*2 phase) and their resulting microstructure also frequently includes secondary phases consisting of the *B*2 or *L*2_1 intermetallic—both of which are particular orderings upon a body centered cubic lattice [3]. Initial attempts to recreate the γ/γ' microstructure via the addition of Al, Ti, and/or Zr to a refractory alloy system typically result in coherent "inverted" *A*2/*B*2 microstructures with the intermetallic *B*2 phase forming the continuous matrix and the disordered *A*2 phase forming the precipitates. However, there have been several promising reports of coherent, or semicoherent, *B*2 precipitates embedded within a disordered *A*2 phase [4,5]. A particularly promising family of Ru-based *B*2 phases—*X*Ru, where *X* = Ti, Nb, Zr, Ta, or Hf—has also gained

considerable interest as a potential precipitate phase within an *A*2 matrix because of its stability above 1200 °C [6].

As these microstructures reminiscent of the γ/γ' microstructure begin to emerge within novel body centered cubic alloys, it is important to recall that the dislocation mechanisms by which shearing occurs within the γ' phase of a Ni-based superalloy are what governs their superior mechanical properties [7,8]. Therefore, there is a need to revisit the deformation mechanisms of the intermetallics that will serve as an analog to the γ' precipitate phase. Considering it is well documented within the γ' literature that the planar faults of the precipitate phase often dictate the observed deformation pathways [9–11], it is expected this will also be the case for body centered cubic derived intermetallics. Within this contribution we therefore revisit the formation energies associated with the potential planar faults that can occur via slip on a {110} plane within the *B*2 intermetallic. Although stable intrinsic stacking faults do not exist in body centered cubic lattices [12], the *B*2 intermetallic is not itself a bcc lattice, but a bcc *derived* lattice. The additional chemical ordering present within a *B*2 intermetallic therefore allows for new metastable extended faults that are otherwise not possible within a bcc lattice. These extended faults often correspond to regions wherein a dislocation has dissociated into two partials bounded by
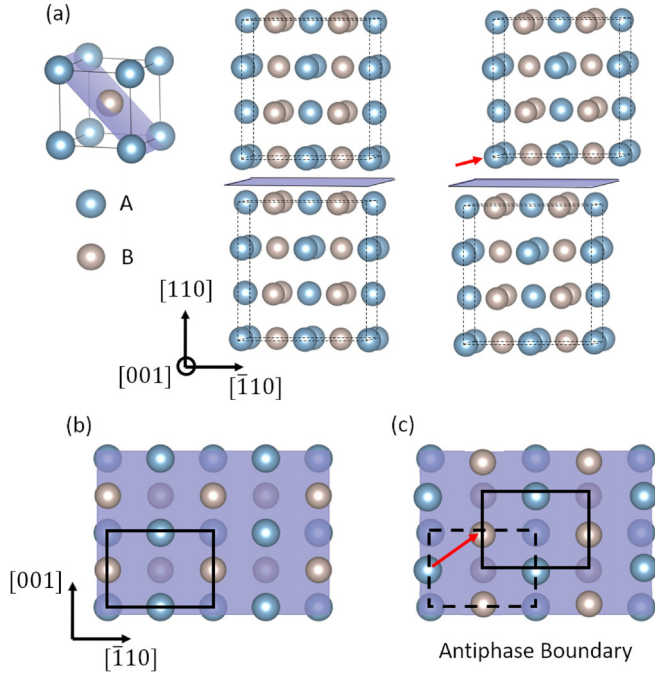
FIG. 1. The formation of an antiphase boundary created via shear within a {110} plane. (a) Orienting the pristine $B2$ structure, shown on the left, along the [110] plane highlighted in purple, clearly reveals the pristine stacking along the [110] direction. One can then imagine shearing one half of the crystal relative to the other by an arbitrary displacement vector shown in red. This, in general, leads to a fault along the [110] direction. When comparing (b) the top down view of the pristine stacking along the [110] direction to (c) the stacking after a shear displacement vector of $\frac{1}{2}[\bar{1}11]$ (red arrow) is applied to the top half of the crystal (with a unit cell outlined by the solid black rectangle) relative to the bottom half of the crystal (with a unit cell outlined by the dashed black rectangle), it becomes clear that nearest neighbor bonds between A and B atoms have been formed that are not present within the pristine ordering. This signifies the formation of an antiphase boundary. Of course this process can occur in any 110 plane; the antiphase boundary of the $B2$ intermetallic is therefore referred to as a $\frac{1}{2}\langle 111\rangle\{110\}$ antiphase boundary.

an extended fault with a stacking that corresponds to the atomic configuration of a $\frac{1}{2}\langle 111\rangle\{110\}$ antiphase boundary. This antiphase boundary, relative to the pristine ordering of the $B2$ intermetallic, is a shear-type antiphase boundary produced by dislocation glide along a {110} plane within the $B2$ crystal structure and is described schematically in Fig. 1. This particular atomic configuration occurs when one half of a $B2$ crystal is displaced by $\frac{1}{2}\langle 111\rangle$ relative to the other half of the crystal along a {110} plane. Interestingly, slip on the {110} plane within $B2$ intermetallics often involves dislocations with a Burgers vector of either $\langle 001\rangle$ or $\langle 111\rangle$. The observed slip direction is believed to be determined by the dissociation of either the $\langle 001\rangle$ or $\langle 111\rangle$ Burgers vector into two partial dislocations that bound an antiphase boundary described by the atomic configuration shown in Fig. 1(c). Based on this analysis, which has been discussed in detail by Lin *et al.* [13], the antiphase boundary energy, along with the elastic constants of a particular $B2$ intermetallic, may determine its experimentally observed slip direction.

The present paper aims to develop a computationally efficient *ab initio* model that can rapidly assess antiphase boundary energies as a function of composition within the $B2$ intermetallic. Specifically, we adopt the diffuse multilayer fault model (DMLF) initially proposed by Vamsi and Karthikeyan for $L1_2$ compounds [14] and further extended by the work of Vamsi and Pollock [15]. The diffuse multilayer fault model, which identifies proximate structures that best capture the bonding environment within the layers adjacent to an antiphase boundary of interest, can then be used to predict the planar fault energies of multicomponent $B2$ intermetallics that may be found in experimentally relevant multicomponent alloy systems. Upon validating the proximate structures identified for the $B2$ intermetallic, we study the influence of composition on (i) the antiphase boundary energies within $Hf_{1-x}Ti_xRu$ and $Hf_{1-x}Al_xRu$ and (ii) the expected fault width of an antiphase boundary for each of the compositions studied. Finally, due to the large number of material systems that are studied here, we also present a brief discussion on how the d-d orbital interactions within a number of $B2$ intermetallics influence their relative chemical stability.

II. METHODS

As outlined in Fig. 1, one can mathematically construct an antiphase boundary as a union between two semi-infinite single crystals (of a particular intermetallic) that are translational variants of one another. There are two noteworthy consequences of this fact.

(i) The resulting atomic configuration is a distinct ordering on the lattice upon which the intermetallic is "derived."

(ii) Any changes in the energetics of this atomic configuration—relative to a pristine infinite single crystal of the intermetallic—are short range.

Therefore most of the chemical environments present within this faulted crystal remain unchanged and, in theory, the energy penalty associated with the formation of the antiphase boundary can be captured by the change in bonding environment within the first few layers adjacent to the fault. Therefore, identifying proximate structures which have similar bonding to the bonding found within planes adjacent to an antiphase boundary should reasonably approximate the energetics of the antiphase boundary.

Since an antiphase boundary within the $B2$ intermetallic is a distinct ordering on the bcc parent lattice upon which it is derived, proximate crystal structures for each layer of the antiphase boundary can be identified via a "least-squares" metric. Specifically, to identify the proximate structure for the L_ith layer adjacent to the antiphase boundary, our metric evaluates the bonding environment in the L_ith layer relative to a particular bonding environment of a symmetrically distinct atomic ordering upon a bcc lattice that preserves the stoichiometry of the $B2$ intermetallic. This metric, termed Π^t, evaluated for layer L_i relative to a symmetrically distinct atomic ordering, S_q, is defined as

$$\Pi^t(L_i, S_q) = \sqrt{\Sigma_{j=1}^M \frac{1}{2d_j^2}\Sigma_{u,v}\Delta N_j^{uv}(L_i, S_q)} \qquad (1)$$

where ΔN_j^{uv} is defined as a dot product between the difference in the number of uv bonds present at the interatomic distance
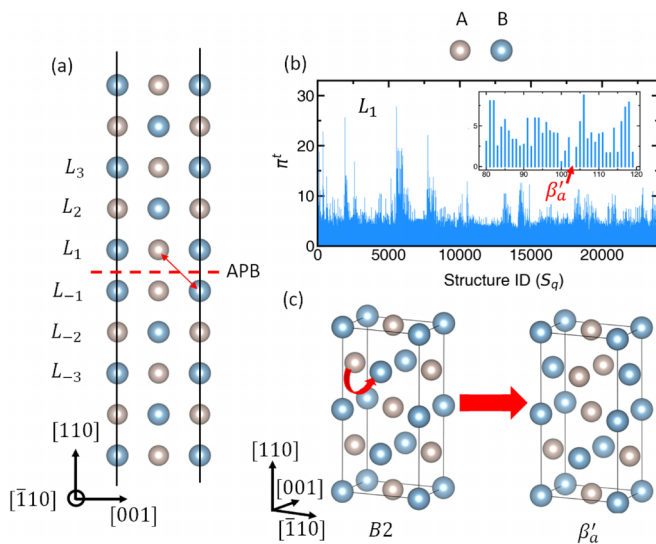
FIG. 2. The workflow used to identify each proximate structure. (a) The atomic configuration that corresponds to the antiphase boundary is generated and each layer adjacent to the fault is labeled. Note that the layers come in pairs, i.e., $L_1 \equiv L_{-1}$. (b) Each symmetrically distinct atomic ordering, S_q, is enumerated with the help of CASM and is evaluated against the bonding environment of a particular layer, in this case, L_1, based on the metric Π^t. For L_1, there is in fact one atomic configuration (red arrow) within the database that is identical to the L_1 bonding environment up to the tenth nearest neighbor labeled β'_a. (c) The proximate structure for L_1, β'_a, is compared to the pristine ordering of the $B2$ structure along the {110} plane. The β'_a structure is a simple one atom permutation relative to the $B2$ ordering.

j within the atomic configuration of the bcc lattice being considered:

$$\Delta N_j^{uv}(L_i, S_q) = \left[N_j^{uv}(L_i) - N_j^{uv}(S_q) \right]^2 \quad (2)$$

where u and v therefore range over the distinct elements present within the intermetallic (specifically for the $B2$ intermetallic u, v $\in$ $[A, B]$) and j ranges over pairwise interactions up to the Mth next nearest neighbors. Each ΔN_j^{uv} is weighted by its respective jth interatomic distance, d_j, in order to ensure that the proximate structure identified for each layer adjacent to the fault preferentially minimizes the ΔN_j^{uv}'s with the smallest interatomic distances. The Clusters Approach to Statistical Mechanics (CASM) software package [16,17] was used to enumerate a complete database of symmetrically distinct orderings, with up to 40 atomic sites, for the $B2$ intermetallic. The maximum number of Mth nearest neighbors to be considered when computing Π^t is then chosen to be 10 so that it is sufficiently large enough to capture all pairwise interactions that may significantly contribute to the energy penalty associated with the formation of an antiphase boundary. The general workflow of this method applied to the $B2$ intermetallic is summarized within Fig. 2.

The diffuse multilayer fault model developed via the workflow outlined above is then validated against the antiphase boundary energies predicted by antiphase boundary containing supercells that were generated with the software package MULTISHIFTER [18] for a number of experimentally

relevant $B2$ intermetallics that, according to the Open Quantum Materials Database [19,20], are stable at $T = 0$ K.

Upon validation of the diffuse multilayer fault model, further studies are performed wherein a third element is substituted onto one of the sublattices of the $B2$ intermetallic to create pseudobinary intermetallics with a general composition of $A_{1-x}A'_xB$. Specifically, we choose to study $\mathrm{Hf}_{1-x}\mathrm{Ti}_x\mathrm{Ru}$ and $\mathrm{Hf}_{1-x}\mathrm{Al}_x\mathrm{Ru}$ because of their recently reported promise as precipitate phases within an $A2$ refractory alloy matrix above 1200 °C [6]. We assume complete disorder on the A site of the intermetallic and therefore employ special quasirandom structures [21], generated via a Monte Carlo simulated annealing algorithm [22] that is included in the ATAT software package [23], to model the properties of these pseudobinary alloys. Special quasirandom structures are identified for both the $B2$ structure and the proximate structures required for the diffuse multilayer fault model at compositions of $x = 0.25$, 0.50, and 0.75.

For each $B2$ intermetallic, elastic constants are also computed from first principles in order to predict fault widths found within these material systems. The elastic constants C_{11}, C_{12}, and C_{44} are determined via the energy-strain method provided in AELAS [24] using the primitive cell of the $B2$ crystal structure. Additionally, to investigate trends in chemical stability, crystal orbital Hamilton populations are calculated via the software package LOBSTER based on self-consistent static calculations on a subset of $B2$ intermetallics [25–28].

Both the antiphase boundary energy calculation based on the diffuse multilayer fault model and the supercell method are performed within VASP [29] using projector-augmented-wave pseudopotentials [30,31] and the Perdew-Burke-Ernzerhof generalized gradient approximation [32]. The equilibrium lattice parameter of each intermetallic is first determined by a complete structural relaxation where the unit cell shape, unit cell volume, and ion positions are permitted to vary. The energy of each proximate structure required for the calculation of the antiphase boundary energy based on the diffuse multilayer fault model is then calculated based on proximate structures with the lattice parameter determined from the structural relaxation. In this calculation only ion positions are permitted to relax. The diffuse multilayer fault model antiphase boundary energy is then calculated as

$$\gamma_{\mathrm{DMLF}}^{\mathrm{APB}} = \rho \Sigma [E(S_i) - E(P)] \approx \rho \Sigma_{i \geqslant 1} [E(S_i) - E(P)] \quad (3)$$

where the sum is over all layers adjacent to the fault with a bonding environment that is captured by a proximate structure, S_i, that differs from that of the pristine structure, P. The term ρ corresponds to the number of atoms within the plane of the fault per unit area. For the $B2$ intermetallic $\rho = 2/\sqrt{2}a_0^2$ where a_0 is the lattice parameter of the particular $B2$ intermetallic being studied.

For the supercell calculations, periodic images of an antiphase boundary were separated by greater than 16 Å and only structural relaxation normal to the plane of the fault was allowed. The antiphase boundary energy is then calculated as

$$\gamma_{\mathrm{supercell}}^{\mathrm{APB}} = \frac{1}{2\sqrt{2}a_0^2}[E(\mathrm{supercell}) - E(\mathrm{pristine})]. \quad (4)$$
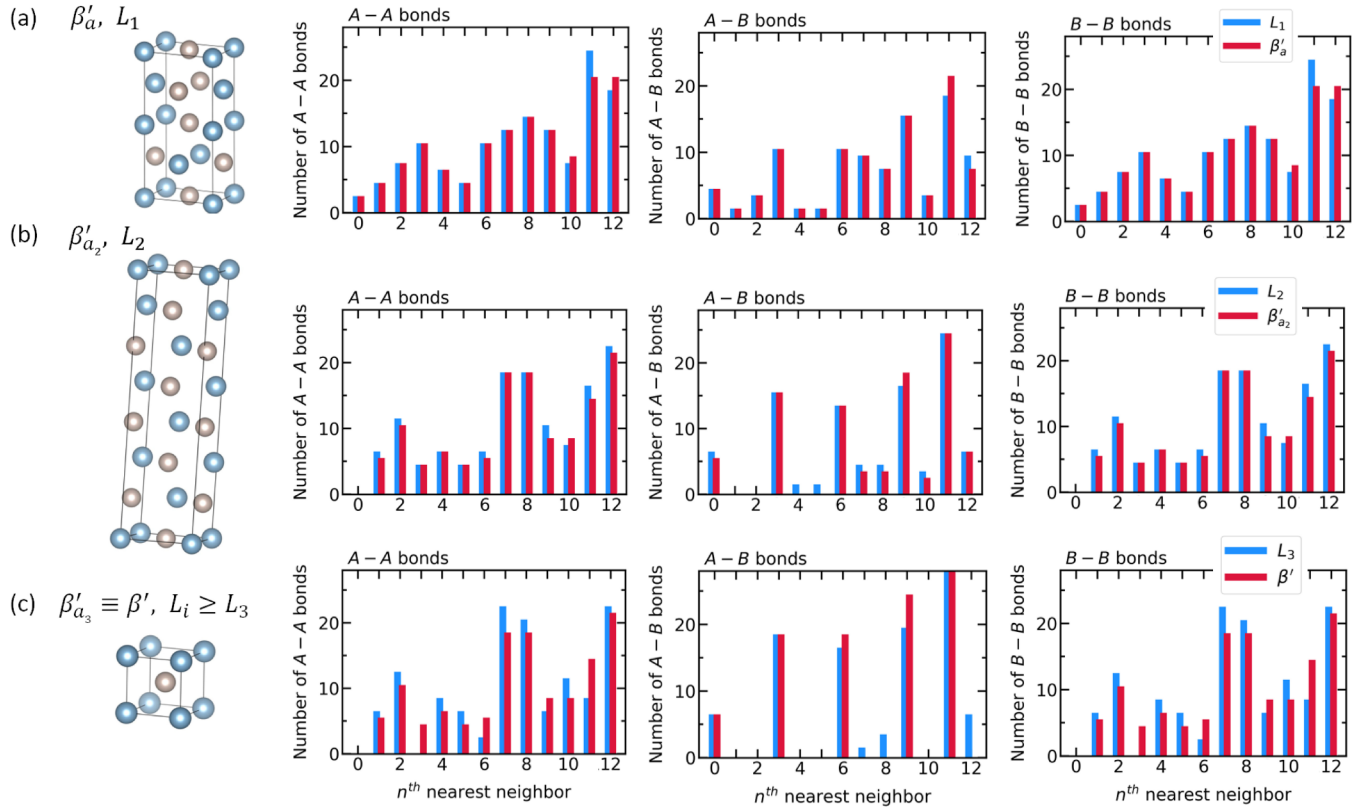
FIG. 3. A comparison of the number of each bond type present within the first three layers adjacent to the $\frac{1}{2}\langle 111\rangle\{110\}$ antiphase boundary of the $B2$ intermetallic and each layer's corresponding proximate structure. (a) The structure β'_a best approximates the bonding environment of L_1 with an identical bonding environment up to tenth nearest neighbor. (b) β'_{a_2} best approximates the bonding environment of L_2 with nearly identical bonding that leads to a Π^t value of 0.746. (c) The third layer, and therefore all layers further from the fault, are best approximated by the pristine $B2$ stacking. While there are noticeable differences in bonding environment the Π^t metric is only 1.05.

Spin polarization was included within all calculations and a Monkhorst-Pack scheme was used to construct the Brillouin zone [33]. A $15 \times 15 \times 15$ k-point grid was used for the initial structural relaxation of the pristine intermetallics; all further calculations then use grids that are scaled accordingly in order to preserve this k-point density.

III. RESULTS AND DISCUSSION

A major incentive for developing, and validating, the diffuse multilayer fault model for the $B2$ intermetallic is the fact that this model can be used to predict the change in antiphase boundary energy within multicomponent intermetallics [15,34]. In the following section we demonstrate that the diffuse multilayer fault model successfully predicts the $\frac{1}{2}\langle 111\rangle\{110\}$ antiphase boundary energy of numerous binary $B2$ intermetallics. We then use the diffuse multilayer fault model to explore the effect of elemental substitution on antiphase boundary energetics. The fault widths within $Hf_{1-x}Ti_xRu$ and $Hf_{1-x}Al_xRu$ are also approximated based on the computed elastic constants and antiphase boundary energies. We conclude with a brief discussion on the correlation between $B2$ stability and antiphase boundary energies within this material class.

A. Diffuse multilayer fault model validation

Figure 3 summarizes the diffuse multilayer fault model corresponding to the $\frac{1}{2}\langle 111\rangle\{110\}$ antiphase boundary that can form within a $B2$ intermetallic. Following the nomenclature of Vamsi and Pollock for the antiphase boundary of the γ' $L1_2$ intermetallic [15], the two proximate structures for the first and second layers adjacent to the $\frac{1}{2}\langle 111\rangle$ $B2$ antiphase boundary have been termed β'_a and β'_{a_2}, respectively. As shown in Fig. 3, only two proximate structures are needed because the bonding environment of all other layers adjacent to the fault is best captured by the pristine $B2$ crystal structure. The bonding environment of β'_a is summarized in Fig. 3(a), demonstrating that the bonding environment of this proximate structure is identical to the bonding environment of the first layer of the antiphase boundary up to the tenth nearest neighbor pairwise interaction—suggesting that this structure will provide a reliable evaluation of the energy penalty associated with the first term of the summation in Eq. (3). The bonding environment of the second layer adjacent to the antiphase boundary is best captured by β'_{a_2}, as summarized within Fig. 3(b). While β'_{a_2} does contain differences in the number of particular chemical interactions at each of the first three nearest neighbors, Π^t is near zero with a value of 0.746. For the third layer adjacent to the antiphase boundary—and therefore all layers further from the fault as well—the proximate structure is identified as the bonding environment found

within the pristine *B*2 structure. Similar to layer 2, the bonding environment in the pristine *B*2 intermetallic (β') is not identical to that of layer 3, but a Π^t of 1.05 reflects the minor changes in bonding environment that are tabulated in Fig. 3(c).

Upon inspection of Fig. 3 as a whole, several characteristics of the diffuse multilayer fault model become apparent. The first is that when identifying a proximate structure for layers further from the fault, larger nearest neighbor distances articulate the presence of an antiphase boundary within the crystal structure that is being approximated by the diffuse multilayer fault model. This is advantageous because if the bonding environments that differ from the pristine *B*2 structure occur at larger nearest neighbor distances for larger L_i's, then the *i*th energy contribution computed via Eq. (3) becomes smaller. However, the importance of larger nearest neighbor distances also means that the best proximate structure for higher order L_i's will require proximate structures with a larger number of atomic sites. Even so, the goal of the diffuse multilayer fault model is to compute the antiphase boundary energy of compositionally complex *B*2 intermetallics in a computationally efficient manner; therefore, as discussed in the methods, only symmetrically distinct atomic configurations with up to 40 atomic sites are considered as candidate proximate structures. This database is searched, and based on Π^t a reasonably sized structure is identified as the best proximate structure for layer L_i. Figure 3 demonstrates that once L_3 is reached there is no candidate structure better at capturing the bonding environment of this layer of the antiphase boundary than the pristine *B*2 intermetallic ordering—this is therefore the critical layer (at least when considering only symmetrically distinct atomic configurations with up to 40 atomic sites) where the layer, and all $L_i > 3$, appear to have a local atomic configuration nearly identical to that of the *B*2 intermetallic. Of course it will take several layers beyond L_3 for the number of *A*-*A*, *A*-*B*, and *B*-*B* bonds within the pristine *B*2 intermetallic to match the true bonding environment of the layer being considered, but as previously discussed, the *i*th energy contribution computed via Eq. (3) for $L_i \geqslant L_3$ is significantly smaller than the energy contribution of L_1 and L_2.

Ultimately, if the diffuse multilayer fault model of Fig. 4 reliably reproduces the antiphase boundary energies computed via the density functional theory (DFT) supercell method, then it can be applied to compositionally complex *B*2 intermetallics. The proximate structures provided within Fig. 3 have therefore been employed to estimate antiphase boundary energies of a number of experimentally relevant *B*2 intermetallics that, according to the Open Quantum Materials Database [19,20], are stable at $T = 0$ K and have been validated against the antiphase boundary energy determined via the DFT supercell method. The correlation between the diffuse multilayer fault method and the DFT supercell method is shown in Fig. 4. While the best fit line, $\gamma_{\text{supercell}}^{\text{APB}} = A\gamma_{\text{DMLF}}^{\text{APB}} + \gamma_0$ ($A = 0.85$, $\gamma_0 = 47.08 \text{ mJ/m}^2$), is not the "unity line" $\gamma_{\text{supercell}}^{\text{APB}} = \gamma_{\text{DMLF}}^{\text{APB}}$, the energies of the diffuse multilayer fault model are strongly correlated ($R^2 = 1$, RMSE = 52 mJ/m^2) to the energies computed by the supercell method. The predictive power of the diffuse multilayer fault model for the $\frac{1}{2}\langle 111\rangle\{110\}$ antiphase boundary is therefore clear and allows
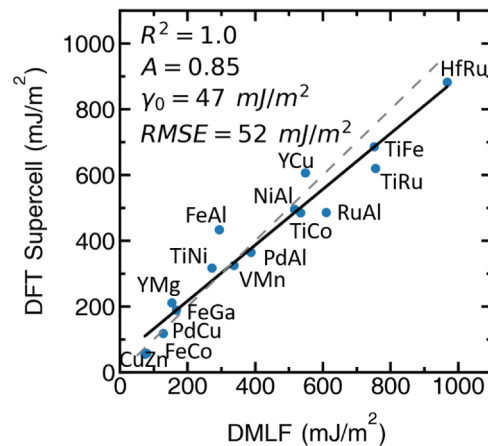

FIG. 4. Validation of the diffuse multilayer fault model against DFT supercell calculations. While the (solid) line does not have a slope of unity (dashed), there is a clear correlation between the antiphase boundary energies predicted by the diffuse multilayer fault model and that of DFT supercell calculations. This confirms the predictive power of the diffuse multilayer fault model which can now be used to study the impact of elemental substitution on antiphase boundary energies.

for a computationally efficient estimation of the antiphase boundary energy for a wide range of multicomponent *B*2 intermetallics.

B. Evaluating antiphase boundary energies and fault widths in *B*2 intermetallics

As previously mentioned, the diffuse multilayer fault model provides a computationally efficient approach to evaluating antiphase boundary energies for multicomponent intermetallics. This enables us to determine to what extent elemental substitution impacts both antiphase boundary energies and fault widths within experimentally relevant *B*2 intermetallics. We approximate antiphase boundary fault widths using anisotropic elasticity theory—similar to the process discussed by Lin *et al.* [13]. In short, assuming that a dislocation lying on a {110} plane within a *B*2 intermetallic with a Burgers vector of either $\langle 001\rangle$ or $\langle 111\rangle$ can dissociate into two partial dislocations with Burgers vectors of $\frac{1}{2}\langle 111\rangle$ and $\frac{1}{2}\langle \bar{1}\bar{1}1\rangle$ or two $\frac{1}{2}\langle 111\rangle$ Burgers vectors, respectively, one can evaluate the fault width of the resulting antiphase boundary by balancing the elastic forces created by the dissociated Burgers vector against the attractive force generated by the formation of an energetically unfavorable antiphase boundary between the two partials. The analytical form of the stress field due to a straight dislocation within an anisotropic medium with cubic crystal symmetry was originally worked out by Eshelby *et al.* who noted that there exist simple solutions to this problem when the plane normal to the dislocation line is of evenfold symmetry [35]. When this plane is of evenfold symmetry, the stress field created by the dislocation of interest can be separated into edge and screw components, ultimately allowing for an analytical prediction of the fault width between partial dislocations, assuming a dissociation event will occur. Interestingly, if the dislocation line lies along the $\langle 111\rangle$ or

TABLE I. Expected fault widths in pristine $B2$ intermetallics. $A_r = \frac{2C_{44}}{C_{11}-C_{12}}$ is the Zener ratio.

Material	C_{11} (GPa)	C_{12} (GPa)	C_{44} (GPa)	A_r	$\gamma^{\mathrm{APB}}(\mathrm{mJ\,m^{-2}})$	$r_{001}^{\mathrm{FW}}/a_0$	$r_{111}^{\mathrm{FW}}/\sqrt{3}a_0$
TiCo	222.4	135.6	61.7	1.42	496	0	2.05
PdCu	174.9	146.3	91.6	6.4	118	1.35	3.51
CuZn	127.3	104.1	77.8	6.73	55	2.06	4.02
FeAl	254.5	136.7	140.1	2.38	433	0.09	5.15
FeCo	265.2	151.5	129.5	2.28	57	0	12.64
FeGa	226.2	145.8	120.0	2.98	211	0	6.34
TiFe	380.4	97.0	73.8	0.52	620	0	3.30
HfRu	374.3	108.1	78.7	0.59	883	0	2.84
VMn	488.8	120.2	93.2	0.51	325	0	8.55
NiAl	206.2	134.7	118.0	3.30	485	0.16	2.07
TiNi	178.4	139.9	50.3	2.61	318	0	1.97
PdAl	189.9	136.6	75.0	2.82	365	0	2.09
RuAl	316.5	147.1	125.7	1.48	486	0	3.53
TiRu	422.6	112.8	88.7	0.57	686	0	3.93
YCu	112.1	51.5	37.2	1.23	187	0	1.51
YMg	53.1	36.0	39.2	4.60	778	0.72	1.90

$\langle 121 \rangle$ direction (which are the crystallographic dislocation line directions relevant for screw and edge dislocations lying on a {110} slip plane with a Burgers vector of $\langle 111 \rangle$, respectively) the plane normal to the dislocation line is *not* a plane of evenfold symmetry. The analysis then proves to be slightly more cumbersome, but an analytical solution does exist for the $\langle 111 \rangle$ dislocation line based on work by Stroh [36] and Head [37]. For this reason, we limit ourselves to the prediction of fault widths of screw dislocations within the {110} plane with Burgers vectors of either $\langle 001 \rangle$ or $\langle 111 \rangle$. Based on the intuition that can be gained from isotropic elasticity theory, fault widths for screw dislocations should be smaller than their edge counterparts and therefore provide a lower bound on the fault width that can be expected to be observed in an experimental study. The complete analyses used for each of the dislocation configurations studied here are included within the Appendix.

The results for the pristine $B2$ intermetallics studied within this contribution are summarized within Table I. Perhaps the most notable finding of these calculations is the fact that the expected fault widths for both $\langle 001 \rangle$ and $\langle 111 \rangle$ screw dislocations in YCu and YMg are near zero—if not exactly zero. This is very interesting considering that these material systems are known to demonstrate significant ductility [38]. In fact, it is often argued that a significant fault width is required to ensure that the dislocation core of a $\langle 111 \rangle$ screw dislocation within a bcc-based material is planar, and therefore more mobile, than an otherwise nonplanar $\langle 111 \rangle$ screw dislocation that spreads onto the three {110} planes that intersect one another [13,39]. This thought process has been used to rationalize both the observed slip systems within a particular $B2$ intermetallic as well as whether the intermetallic is expected to be ductile. While this explanation seems promising, and particularly reasonable because of the role fault widths play in the plastic response of conventional fcc and hcp metals, the results shown here suggest that the explanation for why certain $B2$ intermetallics slip along the $\langle 001 \rangle$ direction and others slip along the $\langle 111 \rangle$ is more subtle. While it is beyond the scope of the current paper to provide a more satisfactory explanation, ongoing efforts

by several of the authors are focused on understanding which slip modes can be expected to be active within particular $B2$ intermetallics across specific temperature regimes. Even so, it is important to stress that dislocations with an $\langle 001 \rangle$ Burgers vector should, in general, not be expected to dissociate. This can be explained by the fact that the attractive edge components of the potential $\frac{1}{2}\langle 111 \rangle$ and $\frac{1}{2}\langle \bar{1}\bar{1}1 \rangle$ partial dislocations outweigh the repulsive screw components in all but PdCu and CuZn. A more detailed discussion is provided within the Appendix.

C. Evaluating antiphase boundary energies and fault widths in pseudobinary $B2$ intermetallics

We also use the proximate structures identified for the $\frac{1}{2}\langle 111 \rangle\{110\}$ antiphase boundary of the $B2$ intermetallic to model the pseudobinary $B2$ intermetallics $\mathrm{Hf}_{1-x}\mathrm{Al}_x\mathrm{Ru}$ and $\mathrm{Hf}_{1-x}\mathrm{Ti}_x\mathrm{Ru}$. As previously discussed in the methods section, special quasirandom structures, based on the layer 1 and layer 2 proximate structures identified in Sec. III A, are used to determine the expected antiphase boundary energy for each multicomponent $B2$ intermetallic. Special quasirandom supercells of the conventional $B2$ ordering are generated because the energy and corresponding elastic constants of this atomic configuration are necessary inputs for Eq. (3) and the prediction of fault widths. The number of atoms required for each special quasirandom structure is determined based on the requirement that the first ten nearest neighbor pair-correlation functions recreate these correlations within random alloys of the same composition. For conventional $B2$ ordering within these pseudobinary intermetallics, this requirement resulted in special quasirandom structures of eight atoms for a composition of $x = 0.25$ and 0.75 and 12 atoms for a composition of $x = 0.50$. The layer 1 proximate structure (β'_{a_1}) required 32 atoms for a composition of $x = 0.25$ and 0.75 and 16 atoms for a composition of $x = 0.50$ while the layer 2 proximate structure (β'_{a_2}) required 56 atoms for a composition of $x = 0.25$ and 0.75 and 28 atoms for a composition of $x = 0.50$.
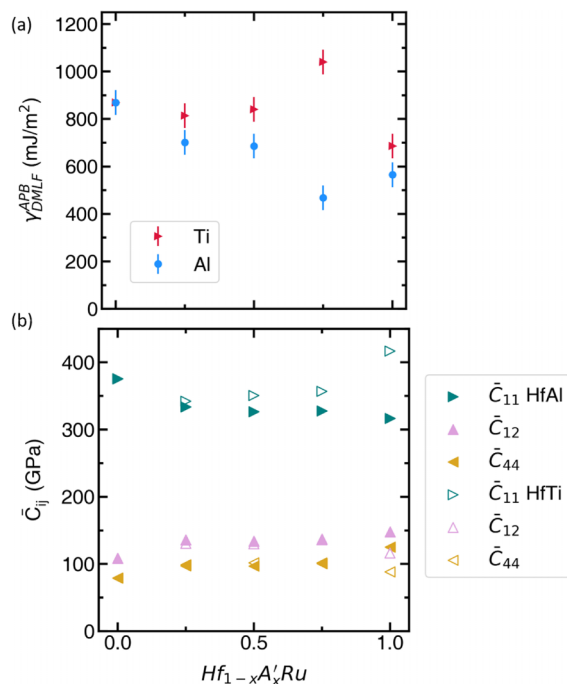
FIG. 5. Antiphase boundary energies (a) and average elastic constants pertaining to cubic symmetry (b) within multicomponent *B*2 intermetallics. While elemental substitution does not appear to significantly impact the elastic properties of the intermetallic, antiphase boundary energies can vary by up to almost 200 mJ/m².

All special quasirandom structures are provided within the Supplemental Material [40].

The impact of elemental substitution on the antiphase boundary energies, as well as the elastic constants for each of the pseudobinary *B*2 intermetallics, are shown within Fig. 5. Interestingly, a maximum in the antiphase boundary energy occurs at $x = 0.75$ for $\text{Hf}_{1-x}\text{Ti}_x\text{Ru}$ while a minimum occurs within $\text{Hf}_{1-x}\text{Al}_x\text{Ru}$ at this same composition. While the uncertainty based on the RMSE value of the diffuse multilayer fault model suggests that the antiphase boundary energy of $\text{Hf}_{0.25}\text{Al}_{0.75}\text{Ru}$ may overlap with that of RuAl, it does appear that elemental substitution of Hf into TiRu significantly increases the antiphase boundary energy. As will be discussed further in the next section, it is expected that the ordering tendency in HfRu is stronger than that of TiRu. This fact may explain why adding Hf to TiRu leads to a significant increase in the energy penalty associated with a stacking fault relative to the pristine order of the multicomponent intermetallic. Specifically, the initial incorporation of Hf into the TiRu antiphase boundary may lead to energetically unfavorable Hf–Ti interactions that destabilize the antiphase boundary atomic configuration relative to the multicomponent *B*2 ordering. However, as more Hf is introduced into the fault, the antiphase boundary energy decreases relative to $\text{Hf}_{0.25}\text{Ti}_{0.75}\text{Ru}$ because, on average, there are more Hf-Ru interactions than the energetically unfavorable Hf-Ti interaction. The same behavior is not observed for the elastic constants because Hf is isoelectronic to Ti. Therefore, when Hf is substituted onto the Ti sublattice of TiRu, there are no abnormal Hf-Ti interactions analogous to those found within the atomic configuration of

TABLE II. Energy of formations, and expected fault widths in pseudobinary *B*2 intermetallics. $A_r = \frac{2C_{44}}{C_{11}-C_{12}}$ is the Zener ratio.

Material	ΔE_f (meV/atom)	γ^{APB} (mJ m^{-2})	$r_{111}^{\text{FW}}/\sqrt{3}a_0$
TiRu		686	3.93
$\text{Hf}_{0.25}\text{Ti}_{0.75}\text{Ru}$	22.6	1040	1.87
$\text{Hf}_{0.50}\text{Ti}_{0.50}\text{Ru}$	29.5	840	2.38
$\text{Hf}_{0.75}\text{Ti}_{0.25}\text{Ru}$	20.9	814	2.38
HfRu		883	2.84
$\text{Hf}_{0.75}\text{Al}_{0.25}\text{Ru}$	−16.3	701	2.85
$\text{Hf}_{0.50}\text{Al}_{0.50}\text{Ru}$	−10.2	686	2.76
$\text{Hf}_{0.25}\text{Al}_{0.75}\text{Ru}$	4.1	468	4.21
AlRu		486	3.53

the antiphase boundary. As a result, the nature of the bonding within $\text{Hf}_{0.25}\text{Ti}_{0.75}\text{Ru}$ remains relatively unchanged in relation to TiRu and the elastic constants are not impacted significantly. Therefore, as a rough estimate—particularly when the sole purpose of computing the elastic constants is to predict fault widths—Vegard's law should suffice.

The predicted antiphase boundary energies, along with the elastic constants of each pseudobinary intermetallic, can then be used to understand whether elemental substitution can be expected to lead to notable changes in the fault width of the antiphase boundary that is bounded by two partial dislocations. The results for the fault widths of an antiphase boundary bounded by two $\frac{1}{2}\langle 111 \rangle\{110\}$ partial dislocations in $\text{Hf}_{1-x}\text{Ti}_x\text{Ru}$ and $\text{Hf}_{1-x}\text{Al}_x\text{Ru}$ are summarized within Table II. While it is beyond the scope of the current paper to identify composition windows of each intermetallic system that are stable at elevated temperatures, all alloy compositions studied prove to be mechanically stable and possess either low formation energies or slightly negative formation energies, with respect to their end members. This suggests that these alloy systems provide a reasonable platform for exploring the main goal of this paper: To develop a reliable platform for efficiently predicting antiphase boundary energies and the associated fault widths as a function of elemental substitution on a particular lattice site of the intermetallic. Based on these results it seems that a change in antiphase boundary energy of approximately 25%, coupled to the slight changes in elastic constants that occur upon elemental substitution, does not play a major role in impacting the experimentally observed fault width. Whether a significant fault width should be expected within a particular multicomponent system can therefore be gauged by the fault width predicted by anisotropic elasticity theory within the end member intermetallics.

While the diffuse multilayer fault model does not explicitly consider the impact of temperature on the antiphase boundary energies, it is possible to gain insight into whether chemical segregation to the antiphase boundary within a particular candidate alloy system can be expected. If, for example, a candidate pseudobinary *B*2 intermetallic demonstrates a fairly constant antiphase boundary energy as a function of composition, then one could anticipate that the composition at the fault would simply reflect the average composition of the specimen being studied experimentally, but if the antiphase
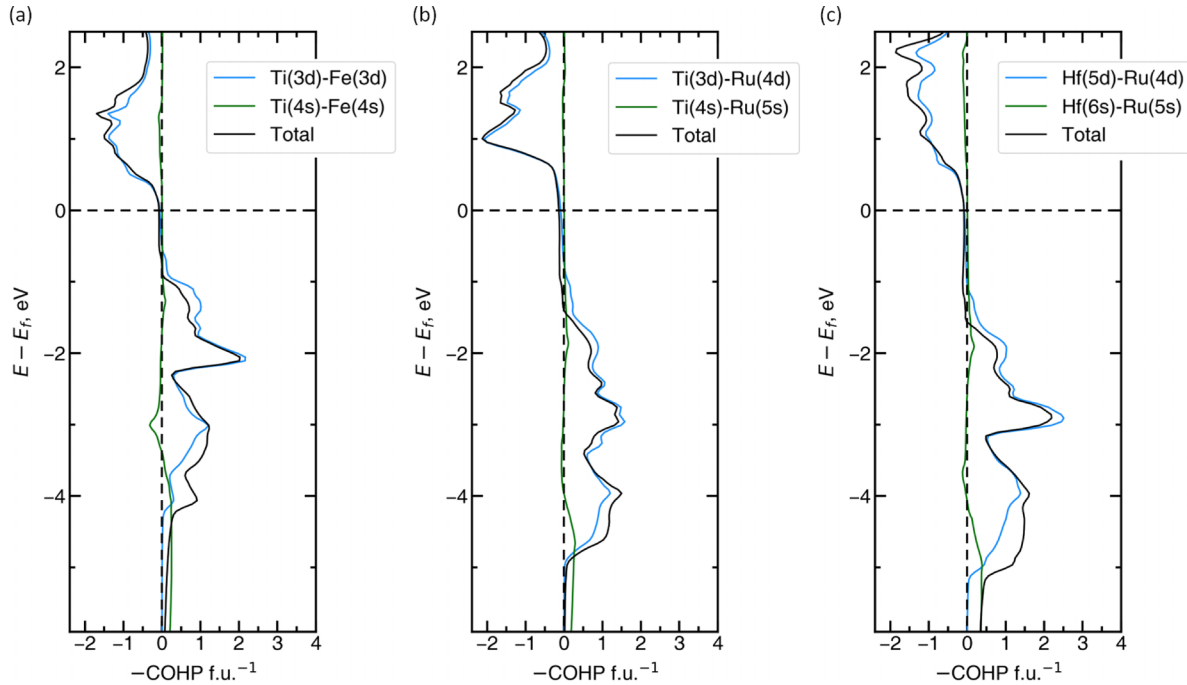
FIG. 6. Projected crystal orbital Hamilton populations (pCOHPs) for TiFe (a), TiRu (b), and HfRu (c). Bonding within these material systems is clearly due to d-d orbital interactions between the two transition metals. All three of these material systems, upon bonding, possess a fully occupied set of d orbitals, which explains their significantly large energy penalties associated with disordered atomic configurations such as the $\frac{1}{2}\langle 111\rangle\{110\}$ antiphase boundary. The energy penalty associated with antiphase boundary formation increases from left to right as the d orbitals become more chemically active within the larger elements that are isoelectronic to either Ti or Fe.

boundary energies are sensitive to composition, then the composition at the antiphase boundary may differ from the average composition of the specimen. As a result, the fact that antiphase boundary energies within both of the pseudobinary systems studied are indeed sensitive to composition suggests that chemical segregation to the antiphase boundary can be expected within both $Hf_{1-x}Ti_xRu$ and $Hf_{1-x}Al_xRu$. Therefore, if $B2$ precipitates similar to the ones studied here are embedded within an $A2$ matrix phase it can be expected that the shearing of these precipitates at elevated temperatures may be coupled to diffusion. In fact, chemical segregation at an antiphase boundary within a complex, multicomponent $B2$ intermetallic containing Ti, Nb, Ta, Zr, Al, and V has been reported experimentally by Couzinié *et al.* [5]. Unfortunately the complexity of the phase reported by Couzinié *et al.* makes it difficult to determine which of these particular elements favor the A site or the B site of the $B2$ lattice. However, the diffuse multilayer fault model developed in this paper for the antiphase boundary of the $B2$ intermetallic now offers a computationally efficient route that can be used to rationalize experimentally observed segregation effects observed in multicomponent $B2$ intermetallics of the form $A_{1-x-y}A'_xA''_yB$ or $A_{1-x}A'_xB_{1-y}B'_y$.

D. *B2* stability and its relation to antiphase boundary energetics

A brief discussion on the relative chemical stability of the $B2$ structure and its relation to antiphase boundary energies is warranted. It is rather noteworthy that within Fig. 4 the material systems with the largest antiphase boundary energies are $B2$ intermetallics composed of two transition metal elements:

HfRu, TiFe, and TiRu. Of course, a higher antiphase boundary energy implies that the pristine $B2$ ordering is significantly more stable relative to alternative disordered atomic configurations. When the $B2$ is composed of two transition metals, the reason for this high stability can be understood based on the expected d-d orbital interactions between these two elements. In fact, this concept has been explored thoroughly by Brewer [41,42] based on a metallic bonding theory originally proposed by Engel [43]. In short, the theories of Engel and Brewer lead to a generalization of the Lewis acid-base theory to the covalent bonding of intermetallics. Using HfRu as an example, one can see that the d^2s^2 electron configuration of Hf along with the d^7s^1 electron configuration of Ru implies that, upon reacting, Ru can utilize Hf's empty d orbitals to produce an extremely stable electron configuration that includes ten bonding d orbitals. Considering Fe is isoelectronic to Ru and Ti is isoelectronic to Hf, this same schematic of the bonding holds true for TiRu and TiFe. The only difference in TiRu and TiFe is the fact that 3d transition metals will have d orbitals that are much less exposed relative to their 4d or 5d counterparts. The stabilizing effect will therefore be less than the effect present within HfRu—as reflected by the lower antiphase boundary energies of TiFe and TiRu relative to HfRu. This phenomenon is beautifully captured by the respective pCOHPs (see methods for calculation details) of TiFe, TiRu, and HfRu shown in Fig. 6. Within all three of these material systems the Fermi energy sits between a set of "bonding/antibonding" orbitals created via d-orbital hybridization of the two transition metals—implying all three of these $B2$ intermetallics are highly stable. The gap between the "bonding/antibonding" orbitals, which is largest for HfRu

and smallest for TiFe, confirms that the *d* orbitals of Hf and Ru are much more exposed than their 3*d* transition metal analogs—prompting HfRu to be the most stable of the *B*2 compounds studied within this contribution.

IV. CONCLUSIONS

In this paper we have extended the diffuse multilayer fault model to the *B*2 intermetallic by identifying proximate structures that reliably predict the energy penalty associated with the formation of a $\frac{1}{2}\langle 111\rangle\{110\}$ antiphase boundary. The model has been used to study the impact alloying has on antiphase boundary energy within pseudobinary *B*2 intermetallics Hf$_{1-x}$Ti$_x$Ru and Hf$_{1-x}$Al$_x$Ru. Antiphase boundary energies are sensitive to composition, thereby influencing the plastic deformation within these *B*2 intermetallics. This is particularly significant for elevated operating temperatures where it is expected that chemical segregation at the fault will prompt diffusion mediated deformation processes. We also employ anisotropic elasticity theory to study fault widths of antiphase boundaries bounded by either two $\frac{1}{2}\langle 111\rangle$ partial dislocations (a total Burgers vector of $\langle 111\rangle$) or a $\frac{1}{2}\langle\bar{1}\bar{1}1\rangle$ and $\frac{1}{2}\langle 111\rangle$ partial dislocation (a total Burgers vector of $\langle 001\rangle$). While the fault width of an antiphase boundary appears to be fairly insensitive to changes in composition for the systems studied here, the fault width across composition space for *B*2 intermetallics highlights two key points.

(i) Dissociation of $\langle 111\rangle\{110\}$ dislocations into partials separated by a large fault width does not seem to unambiguously determine why the $\langle 111\rangle\{110\}$ slip mode is favored in certain intermetallics.

(ii) $\langle 001\rangle$ Burgers vectors should rarely be expected to dissociate into well-defined partials because of the significant attractive forces caused by the opposite signed edge components of the expected $\frac{1}{2}\langle\bar{1}\bar{1}1\rangle$ and $\frac{1}{2}\langle 111\rangle$ partials.

Lastly, we point out the role covalent bonding can play in stabilizing particular *B*2 intermetallics—specifically those that are formed between two transition metal intermetallics such as TiFe, TiRu, and HfRu. A set of fully occupied *d* orbitals can be expected upon the reaction of the two constituent elements within any three of these binary intermetallics via electron count, consistent with the theory developed by Brewer and Engel. We believe these findings will certainly prove useful in the pursuit of identifying a high temperature, *B*2 strengthened, bcc refractory-based superalloy that outperforms conventional Ni-based superalloys.

APPENDIX

Within this Appendix we provide the coordinate systems, and the corresponding expressions, that are required to determine the potential splitting width between the two partials that would bound an antiphase boundary for Burgers vectors of $\langle 111\rangle$ and $\langle 001\rangle$ relevant to the plastic deformation of *B*2 intermetallics on the $\{110\}$ plane. Both problems require the dislocation line to be along the *z* axis of the coordinate system. The solution for the stress fields of the $\langle 111\rangle$ screw dislocation can then be found based on the work of Stroh [36] and Head [37]. The stress field for the $\langle 001\rangle$ screw dislocation follows from the work of Eshelby *et al.* [35].

1. Separation of the energy factor into a screw and edge component

When the dislocation line of a general straight dislocation is oriented along a coordinate axis that is of evenfold symmetry (conventionally the *z* axis) the stress fields generated by the dislocation can be separated into an edge component and a screw component. The potential splitting width between partials bounded by a stacking-fault-like defect can then be expressed as

$$r = \frac{1}{2\pi\gamma^{\mathrm{APB}}}(\vec{b}_{s1}\cdot\vec{b}_{s2}K_s + \vec{b}_{e1_x}\cdot\vec{b}_{e2_x}K_{e_x} + \vec{b}_{e1_y}\cdot\vec{b}_{e2_y}K_{e_y}) \tag{A1}$$

where γ^{APB} is the energy penalty associated with forming the stacking-fault-like defect and $\vec{b}_{si}$ are the vectors corresponding to the portion of the two partials that are along the dislocation line and $\vec{b}_{ei}$ correspond to the portion of the two partials that are perpendicular to the dislocation line. The dot product is used because dislocations of opposite direction attract while dislocations that point in the same direction repel. K_s and K_e are often called "energy factors" and they are a function of the elastic constants within the coordinate system relevant to the dislocation of interest. For dislocation lines that are along an axis of evenfold symmetry these expressions take the following form:

$$K_s = (C'_{44}C'_{55} - C'_{45}C'_{45})^{1/2}, \tag{A2}$$

$$K_{e_x} = (\bar{C}'_{11} + C'_{12})\left(\frac{C'_{66}\bar{C}'_{11} - C'_{12}}{C'_{22}(\bar{C}'_{11} + C'_{12} + 2C'_{66})}\right)^{1/2}, \tag{A3}$$

$$K_{e_y} = (\bar{C}'_{11} + C'_{12})\left(\frac{C'_{66}\bar{C}'_{11} - C'_{12}}{C'_{11}(\bar{C}'_{11} + C'_{12} + 2C'_{66})}\right)^{1/2} \tag{A4}$$

where $\bar{C}'_{11} = (C'_{11}C'_{12})^{1/2}$. The elastic tensor in the reference frame of interest is generated based on a transformation matrix *Q* where

$$C' = Q^T C Q \tag{A5}$$

and *Q* is built from the rotation matrix, *R*, that rotates from conventional reference frame *X* to the relevant reference
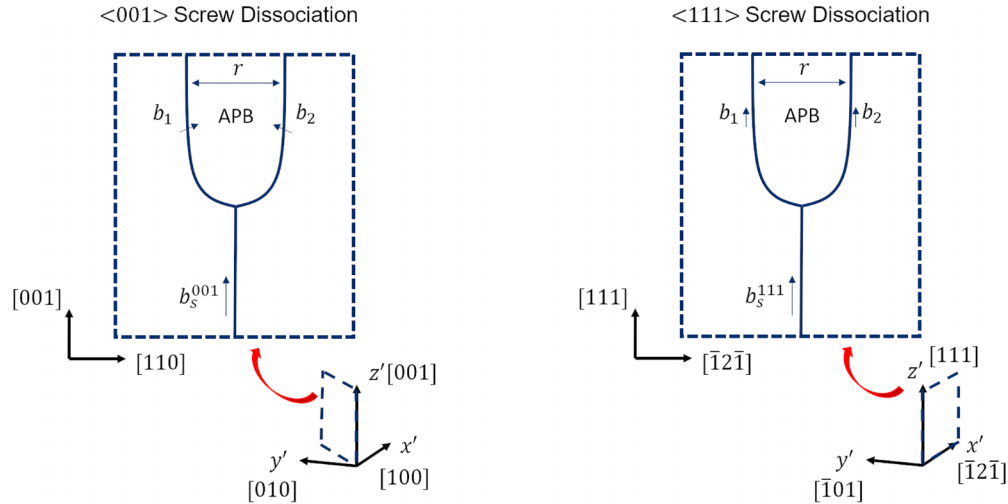
FIG. 7. Potential dissociation events for screw dislocations with a Burgers vector of either $\langle 001 \rangle$ or $\langle 111 \rangle$. For the $\langle 001 \rangle$ screw dislocation, $\vec{b}_1 = \frac{1}{2}\langle 111 \rangle$ and $\vec{b}_2 = \frac{1}{2}\langle \bar{1}\bar{1}1 \rangle$, leading to an attractive force between their edge components. For the $\langle 111 \rangle$ screw dislocation the dissociation simply creates two partial screw dislocations with Burgers vectors of $\vec{b}_1 = \vec{b}_2 = \frac{1}{2}\langle 111 \rangle$.

frame X':

$$R = X' X^{-1}. \tag{A6}$$

Q in matrix form is then

$$Q_{mnkl} = R_{km} R_{ln} \tag{A7}$$

and C'_{ijkl} is

$$C'_{ijkl} = Q^T_{ijgh} C_{ghmn} Q_{mnkl}. \tag{A8}$$

2. Potential $\langle 001 \rangle$ screw dislocation dissociation

The reference frame relevant to the $\langle 001 \rangle$ screw dislocation is simply the conventional reference frame used to describe the cubic elastic constants which means Eqs. (A2)–(A4) simplify to the conventional elastic constants of a cubic crystal. The slip plane intersects the z axis and makes a 45° angle with the x and y axes. A schematic of the dissociation is shown in Fig. 7. Working through the geometry, the final expression for the expected splitting width between partial dislocations is

$$r = \frac{|\vec{b}_s^{001}|^2}{2\pi \gamma^{\text{APB}}} \left(\frac{K_s}{4} - \left[\frac{K_{e_x} + K_{e_y}}{4} \right] \right). \tag{A9}$$

3. Potential $\langle 111 \rangle$ screw dislocation dissociation

The reference frame relevant to the $\langle 111 \rangle$ screw dislocation, shown schematically in Fig. 7, has the z axis aligned

with the [111] direction, the x axis along $[\bar{2}11]$, and the y axis along $[\bar{1}10]$. The analytical form for the energy factor of a screw component, based on the elastic constants rotated into this reference frame [following Eq. (A8)], was worked out by Head [37] based on work originally published by Stroh [36] and is the following:

$$K_s = \frac{M}{S_{44}}, \tag{A10}$$

$$M = \left(\frac{S_{11} S_{44}}{S_{11} S_{44} - S_{15} S_{15}} \right)^{1/2}, \tag{A11}$$

$$S_{11} = \frac{C'_{11} C'_{44} - C'_{15} C'_{15}}{2(C'_{11} + C'_{12})(C'_{44} C'_{66} - C'_{15} C'_{15})}, \tag{A12}$$

$$S_{15} = \frac{-C'_{15}}{2(C'_{44} C'_{66} - C'_{15} C'_{15})}, \tag{A13}$$

$$S_{44} = \frac{C'_{66}}{C'_{44} C'_{66} - C'_{15} C'_{15}}. \tag{A14}$$

The expression for the expected splitting width between partial dislocations is then

$$r = \frac{|\vec{b}_s^{111}|^2}{8\pi \gamma^{\text{APB}}} K_s. \tag{A15}$$

[1] D. B. Miracle and O. N. Senkov, A critical review of high entropy alloys and related concepts, Acta Mater. **122**, 448 (2017).

[2] D. B. Miracle, M.-H. Tsai, O. N. Senkov, V. Soni, and R. Banerjee, Refractory high entropy superalloys (RSAs), Scr. Mater. **187**, 445 (2020).

[3] M. Yamagiuchi, D. Pope, V. Vitek, and Y. Umakoshi, Planar faults and dislocation dissociations in body-centred-cubic-derivative ordered structures, Philos. Mag. A **43**, 1265 (1981).

[4] G. Ghosh and G. Olson, Integrated design of Nb-based super-alloys: *Ab-initio* calculations, computational thermodynamics and kinetics, and experimental results, Acta Mater. **55**, 3281 (2007).

[5] J. P. Couzinié, M. Heczko, V. Mazánová, O. N. Senkov, M. Ghazisaeidi, R. Banerjee, and M. J. Mills, High-temperature deformation mechanisms in a BCC+*B*2 refractory complex concentrated alloy, Acta Mater. **233**, 117995 (2022).

[6] C. Frey, R. Silverstein, and T. M. Pollock, A high stability *B*2-containing refractory multi-principal element alloy, Acta Mater. **229**, 117767 (2022).

[7] T. Pollock and R. Field, Dislocations and high-temperature plastic deformation of superalloy single crystals, Dislocation in Solids **11**, 547 (2002).

[8] Y. Eggeler, K. Vamsi, and T. Pollock, Precipitate shearing, fault energies, and solute segregation to planar faults in Ni-, CoNi-, and Co-base superalloys, Annu. Rev. Mater. Res. **51**, 209 (2021).

[9] M. S. Titus, Y. M. Eggeler, A. Suzuki, and T. M. Pollock, Creep-induced planar defects in $L1_2$-containing Co-and CoNi-base single-crystal superalloys, Acta Mater. **82**, 530 (2015).

[10] V. Vorontsov, L. Kovarik, M. Mills, and C. Rae, High-resolution electron microscopy of dislocation ribbons in a CMSX-4 superalloy single crystal, Acta Mater. **60**, 4866 (2012).

[11] K. Vamsi and S. Karthikeyan, Deformation modes and yield strength anomaly in $L1_2$ compounds, J. Alloys Compd. **860**, 158411 (2021).

[12] V. Vítek, Intrinsic stacking faults in body-centred cubic crystals, Philos. Mag. **18**, 773 (1968).

[13] Y.-S. Lin, M. Cak, V. Paidar, and V. Vitek, Why is the slip direction different in different *B*2 alloys? Acta Mater. **60**, 881 (2012).

[14] K. Vamsi and S. Karthikeyan, High-throughput estimation of planar fault energies in A_3B compounds with L1$_2$ structure, Acta Mater. **145**, 532 (2018).

[15] K. Vamsi and T. M. Pollock, A new proximate structure for the APB (111) in L1$_2$ compounds, Scr. Mater. **182**, 38 (2020).

[16] B. Puchala, J. C. Thomas, A. R. Natarajan, J. G. Goiri, S. S. Behara, J. L. Kaufman, and A. Van der Ven, CASM: A software package for first-principles based study of multicomponent crystalline solids, Comput. Mater. Sci. **217**, 111897 (2023).

[17] A. Van der Ven, J. C. Thomas, B. Puchala, and A. R. Natarajan, First-principles statistical mechanics of multicomponent crystals, Annu. Rev. Mater. Res. **48**, 27 (2018).

[18] J. G. Goiri and A. Van der Ven, MultiShifter: Software to generate structural models of extended two-dimensional defects in 3D and 2D crystals, Comput. Mater. Sci. **191**, 110310 (2021).

[19] J. E. Saal, S. Kirklin, M. Aykol, B. Meredig, and C. Wolverton, Materials design and discovery with high-throughput density functional theory: The open quantum materials database (OQMD), JOM **65**, 1501 (2013).

[20] S. Kirklin, B. Meredig, A. Thompson, J. W. Doak, M. Aykol, S. Rühl, and C. Wolverton, The open quantum materials database (OQMD): Assessing the accuracy of DFT formation energies, npj Comput. Mater. **1**, 15010 (2015).

[21] A. Zunger, S.-H. Wei, L. G. Ferreira, and J. E. Bernard, Special quasirandom structures, Phys. Rev. Lett. **65**, 353 (1990).

[22] A. van de Walle, P. Tiwary, M. de Jong, D. Olmsted, M. Asta, A. Dick, D. Shin, Y. Wang, L.-Q. Chen, and Z.-K. Liu, Efficient stochastic generation of special quasirandom structures, Calphad **42**, 13 (2013).

[23] A. van de Walle, M. Asta, and G. Ceder, The alloy theoretic automated toolkit: A user guide, Calphad **26**, 539 (2002).

[24] S. Zhang and R. Zhang, AELAS: Automatic ELAStic property derivations *via* high-throughput first-principles computation, Comput. Phys. Commun. **220**, 403 (2017).

[25] R. Dronskowski and P. E. Blöchl, Crystal orbital Hamilton populations (COHP): Energy-resolved visualization of chemical bonding in solids based on density-functional calculations, J. Phys. Chem. **97**, 8617 (1993).

[26] V. L. Deringer, A. L. Tchougréeff, and R. Dronskowski, Crystal orbital Hamilton population (COHP) analysis as projected from plane-wave basis sets, J. Phys. Chem. A **115**, 5461 (2011).

[27] S. Maintz, V. L. Deringer, A. L. Tchougréeff, and R. Dronskowski, Analytic projection from plane-wave and PAW wavefunctions and application to chemical-bonding analysis in solids, J. Comput. Chem. **34**, 2557 (2013).

[28] S. Maintz, V. L. Deringer, A. L. Tchougréeff, and R. Dronskowski, LOBSTER: A tool to extract chemical bonding from plane-wave based DFT, J. Comput. Chem. **37**, 1030 (2016).

[29] G. Kresse and J. Furthmüller, Efficient iterative schemes for *ab-initio* total-energy calculations using a plane-wave basis set, Phys. Rev. B **54**, 11169 (1996).

[30] P. E. Blöchl, Projector augmented-wave method, Phys. Rev. B **50**, 17953 (1994).

[31] G. Kresse and D. Joubert, From ultrasoft pseudopotentials to the projector augmented-wave method, Phys. Rev. B **59**, 1758 (1999).

[32] J. P. Perdew, K. Burke, and M. Ernzerhof, Generalized gradient approximation made simple, Phys. Rev. Lett. **77**, 3865 (1996).

[33] H. J. Monkhorst and J. D. Pack, Special points for Brillouin-zone integrations, Phys. Rev. B **13**, 5188 (1976).

[34] K. Vamsi, M. Charpagne, and T. Pollock, High-throughput approach for estimation of intrinsic barriers in FCC structures for alloy design, Scr. Mater. **204**, 114126 (2021).

[35] J. Eshelby, W. Read, and W. Shockley, Anisotropic elasticity with applications to dislocation theory, Acta. Metall. **1**, 251 (1953).

[36] A. Stroh, Dislocations and cracks in anisotropic elasticity, Philos. Mag. **3**, 625 (1958).

[37] A. Head, The [111] dislocation in a cubic crystal, phys. stat. sol. (b) **6**, 461 (1964).

[38] K. Gschneidner Jr, A. Russell, A. Pecharsky, J. Morris, Z. Zhang, T. Lograsso, D. Hsu, C. Chester Lo, Y. Ye, A. Slager, *et al.*, A family of ductile intermetallic compounds, Nat. Mater. **2**, 587 (2003).

[39] V. Paidar and M. Čák, Three types of dislocation core structure in *B*2 alloys, Intermetallics **73**, 21 (2016).

[40] See Supplemental Material at http://link.aps.org/supplemental/10.1103/PhysRevMaterials.8.013610 for the crystallographic information of both the proximate structures and special quasirandom structures used within this work.

[41] L. Brewer, A most striking confirmation of the engel metallic correlation, Acta. Metall. **15**, 553 (1967).

[42] L. Brewer, The generalized Lewis acid-base theory: Surprising recent developments, J. Chem. Educ. **61**, 101 (1984).

[43] N. N. Engel, Alloy phase stability criteria, in *Developments in the Structural Chemistry of Alloy Phases* (Springer, New York, 1969), pp. 25–48.

[44] J. Towns, T. Cockerill, M. Dahan, I. Foster, K. Gaither, A. Grimshaw, V. Hazlewood, S. Lathrop, D. Lifka, G. D. Peterson, R. Roskies, J. Scott, and N. Wilkins-Diehr, XSEDE: Accelerating scientific discovery, Comput. Sci. Eng. **16**, 62 (2014).